

Probing Landau levels of strongly interacting massive Dirac electrons in layer-polarized MoS₂

Jiangxiazhi Lin¹, Tianyi Han¹, Benjamin A. Piot², Zefei Wu¹, Shuigang Xu¹, Gen Long¹, Liheng An¹, Patrick Ka Man Cheung⁴, Peng-Peng Zheng⁴, Paulina Plochocka³, Duncan K. Maude³, Fan Zhang^{4*}, & Ning Wang^{1*}

¹*Department of Physics and Center for Quantum Materials, The Hong Kong University of Science and Technology, Clear Water Bay, Hong Kong, China*

²*Laboratoire National des Champs Magnétiques Intenses, LNCMI-CNRS-UGA-UPS-INSA-EMFL, F-38042 Grenoble, France*

³*Laboratoire National des Champs Magnétiques Intenses, LNCMI-CNRS-UGA-UPS-INSA-EMFL, F-31400 Toulouse, France*

⁴*Department of Physics, The University of Texas at Dallas, Richardson, Texas 75080, USA*

**E-mails: zhang@utdallas.edu; phwang@ust.hk*

Monolayer transition metal dichalcogenides are recently emerged 2D electronic systems with various novel properties, such as spin-valley locking, circular dichroism, valley Hall effects, Ising superconductivity ¹⁻⁵. The reduced dimensionality and large effective masses further produce unconventional many-body interaction effects. Although recent hole transport measurements in WSe₂ indicate strong interactions in the valence bands ⁶⁻⁹, many-body interaction effects, particularly in the conduction bands, remain elusive to date. Here, for the first time, we perform transport measurements up to a magnetic field of 29 T to study the

massive Dirac electron Landau levels (LL) in layer-polarized MoS₂ samples with mobilities of 22000 cm²/(V·s) at 1.5 K and densities of $\sim 10^{12}$ cm⁻². With decreasing the density, we observe LL crossing induced valley ferrimagnet-to-ferromagnet transitions, as a result of the interaction enhancement of the g-factor^{10,11} from 5.64 to 21.82. Near integer ratios of Zeeman-to-cyclotron energies, we discover LL anticrossings due to the formation of quantum Hall Ising ferromagnets¹²⁻¹⁴, the valley polarizations of which appear to be reversible by tuning the density or an in-plane magnetic field. Our results provide compelling evidence for many-body interaction effects in the conduction bands of monolayer MoS₂ and establish a fertile ground for exploring strongly correlated phenomena of massive Dirac electrons.

Semiconducting transition metal dichalcogenides (TMDCs) such as MoS₂, MoSe₂, WS₂, and WSe₂ form a family of layered 2D materials exhibiting novel electronic and optical properties^{1-3,5,15-17}. In monolayer TMDCs, the inversion symmetry is strongly broken, leading to a massive Dirac band structure at the K/K' valleys with nontrivial Berry phase effects²⁻⁴. The spin-orbit coupling (SOC) further splits the two spin subbands in each valley, whereas the spins are quantized along the out-of-plane direction due to the mirror-plane symmetry. Thus, below the energy of intra-valley spin splitting, the subbands are valley degenerate and spin-valley locked (Fig. 1a). Such a remarkable band structure gives rise to the intriguing circular dichroism¹⁻³, valley Hall effects¹⁵, Ising superconductivity⁵, and anomalous Landau level (LL) structure^{4,18} (Fig. 1b).

By contrast, intrinsic bilayer MoS₂ has a restored inversion symmetry and enjoys a spin degeneracy of opposite layers^{19,20}. Because of the vanishing interlayer coupling at the conduction

band edge at the K/K' points ²¹, a backgate voltage V_g can easily induce a potential difference between the two layers ^{19,20,22}, thereby breaking the inversion symmetry and polarizing the electrons to one of the two layers when Fermi level is lower than the potential difference. Therefore, the low energy electron band structure for such a layer-polarized MoS₂ (Fig. 1a) resembles that of monolayer MoS₂ ²⁻⁴, for which it is technically more difficult to achieve high-mobility samples.

When subjected to a perpendicular magnetic field B , the massive Dirac electrons are quantized into anomalous LLs (Fig. 1b) with a cyclotron gap $E_c = \hbar e B / m^*$, where \hbar is the reduced Planck constant, e is the electron charge, and m^* is the effective mass. Notably, the $N = 0$ LLs exist in only one valley. Below the energy of SOC induced spin splitting Δ_{SOC} , the $N \neq 0$ LLs are valley degenerate and spin-valley locked (Fig. 1b). A valley Zeeman effect ^{3,23} can lift the degeneracy by producing a gap $E_Z = g_{LL} \mu_B B$, where g_{LL} is the effective g-factor in the LL structure, and μ_B is the Bohr magneton. The ratio of Zeeman-to-cyclotron energies E_Z / E_c can be strongly enhanced by electron-electron interactions, and the LLs of different valleys would cross each other if $E_Z / E_c > 1$. Based on such LL crossings or the more tantalizing anticrossings, here we examine the strongly interacting behaviors of massive Dirac electrons in the layer-polarized MoS₂.

A bilayer MoS₂ flake was first exfoliated onto a silicon wafer, then identified by optical contrast, and subsequently encapsulated by two insulating hexagonal boron nitride (hBN) layers. The hBN encapsulation protects the MoS₂ from impurity contamination and degradation ^{24,25}. The sandwich structure was patterned and contacted by Ti/Au electrodes ^{24,25}. Figure 1c shows the vertical cross section and optical image of the device. The electrodes are labeled from 1 to 8,

among which 1 and 5 were used as current injection, 2 and 4 as longitudinal voltage probes, and 2 and 8 as Hall voltage probes. The encapsulated device lies on a SiO₂/Si wafer, to which the V_g was applied. All data were obtained by a standard low-frequency lock-in technique at cryogenic temperatures. We fabricated and measured three samples with the same structure, labelled A, B, and C. They show consistent behaviors, and only results from sample C are presented here. (Data of the other two samples are provided in Supplementary Materials ²².)

From the conductance of the n -type field effect channel at 1.2 K (Fig. 1c), the mobility is calculated as $\mu = (dG/dV_g)l/(wC_g) \approx 22000 \text{ cm}^2/(\text{V}\cdot\text{s})$, where $l = 7.6 \text{ }\mu\text{m}$ and $w = 2.6 \text{ }\mu\text{m}$ are the length and width of the channel, respectively, C_g is the gate capacitance determined by the linear relation between V_g and the electron density n ²². The high mobility and low contact resistance allow us to observe Shubnikov-de Haas (SdH) oscillations down to a carrier density as low as $6.3 \times 10^{11} \text{ cm}^{-2}$ ²², which is hitherto the lowest density for few-layer TMDCs. At $B > 10 \text{ T}$, the system is driven into the quantum Hall regime (Fig. 1d): the onset of plateaus are clearly developed in the Hall resistance (R_{xy}), although the minima remain non-zero in the magneto resistance (R_{xx}).

Figure 1e showcases the measured R_{xx} and R_{xy} at $n = 3.52 \times 10^{12} \text{ cm}^{-2}$. The LL filling factors are labeled in blue for R_{xy} by $\nu = (2\pi\hbar/e^2)/R_{xy}$ and in black for R_{xx} by $\nu = 2\pi n\hbar/eB$. Evidently, the LLs are doubly degenerate at $B < 12.5 \text{ T}$, and the degeneracy is lifted at higher B . The 2-to-1 degeneracy lifting is consistent with the expected valley Zeeman effect ^{3,23} of the electrons in the polarized layer. Moreover, the single frequency B_F obtained from Fourier

analysis²² excludes the possible participation of other subbands. The temperature-dependent SdH oscillations further yield $m^* = 0.55 \pm 0.08 m_0$ without obvious dependence on n or B ; this value is comparable to the calculated effective mass¹⁻⁴ of monolayer electrons in the K/K' valleys.

To determine the valley susceptibility (related to E_Z/E_c), one might suggest to apply an in-plane magnetic field that would enhance E_Z without affecting E_c ^{6,12}. In fact, because of the spin splitting and pinning to the out-of-plane direction, the LLs are immune to the in-plane Zeeman field. Thus, the commonly used tilt field method is not applicable to our system^{7,22}. However, for a strongly interacting 2D electron gas, lowering the density n can enhance E_Z/E_c ⁷⁻¹¹. It follows that E_Z/E_c can be determined by using the LL fan diagram, i.e., the mapping of SdH oscillation amplitudes in the n - B space. Figure 2a plots the LL fan diagram, in which a white dashed line separates two different regimes. On the upper left side there are a series of LL crossings and anticrossings with alternating brightness, i.e., between the brighter and dimmer levels. For instance, the red and blue lines mark one pair of anticrossing levels at $\nu = 7$, with the anticrossing point highlighted by the orange oval, which will be discussed in the last part of this paper. By contrast, on the lower right side there are no dimmer levels or crossings.

The alternating brightness (Fig. 2a) can be attributed to the filling of LLs in different valleys by using the *valley-resolved* Lifshitz-Kosevitch (LK) formula^{26,27}:

$$\Delta R_{xx} = 2R_0 \sum_{r=1}^{N_r} \sum_{\sigma=K,K'} \frac{r\lambda}{\sinh(r\lambda)} \exp\left(\frac{-r\pi\hbar}{E_c\tau_\sigma}\right) \cos(r\phi_\sigma) \quad (1)$$

where $\lambda = 2\pi^2 k_B T / E_c$ is the thermal damping, and $\tau_{K,K'}$ are the valley-resolved scattering time. Given the anomalous LL structure for massive Dirac electrons⁴ (Fig. 1b), $\phi_K = 2\pi B_F / B +$

$\pi E_Z/E_c$ and $\phi_{K'} = 2\pi B_F/B - \pi E_Z/E_c - 2\pi$. In Fig. 2b, the left panel displays the experimental ΔR_{xx} (open circles) at $n = 2.26 \times 10^{12} \text{ cm}^{-2}$ and the fitted ΔR_{xx} (purple line) using Eq. (1) with $N_r = 10$; the best fitting yields $E_Z/E_c = 3.5$. The right panel plots the individual contributions to the fitted ΔR_{xx} from each valley; while both become stronger with increasing B , those of valley K' electrons are relatively weaker and cease at $\sim 18 \text{ T}$ or $\nu = 5$. These findings suggest that the dimmer levels (Fig. 2a) and the flat R_{xx} region (Fig. 2b) correspond to LLs in valley K', and, more significantly, that a valley ferrimagnet-to-ferromagnet transition occurs at $\sim 18 \text{ T}$ or $\nu = 5$ for $n = 2.26 \times 10^{12} \text{ cm}^{-2}$. In addition, the fitting indicates a valley-dependent scattering time $\tau_K > \tau_{K'}$ ²², explaining the stronger SdH oscillations in valley K. $\tau_{K,K'}$ obtained by this method have the same order of magnitude with that obtained by a temperature-dependent analysis²².

When E_Z/E_c is a half-integer, LLs of different valleys are alternating and equally spaced in the valley ferrimagnetic regime, yielding R_{xx} minima at all integer filling factors. By contrast, when E_Z/E_c is an integer, LLs of different valleys coincide in the valley ferrimagnetic regime, producing the pronounced signatures only at $\nu = 1, 2, \dots, \nu_c, \nu_c + 2, \nu_c + 4, \dots$. At $\nu \leq \nu_c$ the ground state is a valley ferromagnet. Given the anomalous LL structure for massive Dirac electrons⁴ (Fig. 3e), $\nu_c = \lceil E_Z/E_c \rceil + 1$, where $\lceil \cdot \rceil$ is the ceiling function. Such principles validate the consistency between the fitted $E_Z/E_c = 3.5$ and the observed ferrimagnet-to-ferromagnet transition at $\nu_c = 5$ for $n = 2.26 \times 10^{12} \text{ cm}^{-2}$ (Fig. 3a). Now we use similar transitions in the LL fan diagram to extract the E_Z/E_c values at lower carrier densities. Since the R_{xx} minima are most striking when E_Z/E_c are integers or half integers, we identify that $n = 1.97, 1.55$, and $1.33 \times 10^{12} \text{ cm}^{-2}$ correspond to $E_Z/E_c = 4, 4.5$, and 5, respectively. Figures 3b-3d display the

observed R_{xx} and R_{xy} for these densities, in good agreement with their characteristic LL structures (Fig. 3e).

The effective g-factor in the LL structure can be obtained by $g_{LL} = 2(E_Z/E_c)/(m^*/m_0)$, which is 2 in the large n (non-interacting) limit. In the $B \rightarrow 0$ limit, the effective g-factor for the conduction-band valley Zeeman effect is $g^* = g_{LL} + 2m_0/m^*$, and $2m_0/m^* = 3.64$ arises from the valley magnetic moment of massive Dirac bands²⁸ (which, if $B \neq 0$, would lead to the gap between the lowest LLs in different valleys⁴ (Fig. 1b)). The effective valley susceptibility ($\propto g^*m^*$) can be further obtained: $g^*m^*/m_0 = 3.1$ ($g^* = 5.64$) in the large n limit and $g^*m^*/m_0 = 12$ ($g^* = 21.82$) at $n = 1.33 \times 10^{12} \text{ cm}^{-2}$. (We have assumed $g_{LL} > 0$, i.e., the valley with the $N = 0$ LL shifts down in energy. If $g_{LL} < 0$, then g^*m^*/m_0 would be 0.9 in the large n limit and -12 at $n = 1.33 \times 10^{12} \text{ cm}^{-2}$.) The best fitting in Fig. 3f gives $g^*m^*/m_0 = 3.1 + 10.8n^{-7/10}$, which may be improved in future experiments that can take into account the neglected electron-hole asymmetry²⁹ and minority orbitals²¹. The giant valley susceptibility and its enhancement with decreasing n are most likely due to the electron-electron interactions in our system^{10,11,30,31}. The interaction strength can be indicated by the dimensionless Wigner-Seitz radius $r_s = 1/(\sqrt{\pi n} a_B^*)$ ¹¹, where $a_B^* = 4\pi\epsilon\hbar^2/(m^*e^2)$ is the effective Bohr radius, and $\epsilon \approx 4\epsilon_0$ is the dielectric constant in our sample³². Our studied densities yield $r_s \sim 10$ (Fig. 3f), which is indeed a strong interaction regime¹¹.

At those densities with integer E_Z/E_c , LL anticrossings are also observed, e.g., evidenced by the secondary R_{xx} minima at $\nu = 5, 7, 9$, and 11 in Fig. 4b for $n = 3.24 \times 10^{12} \text{ cm}^{-2}$ ($E_Z/E_c = 3$).

By applying our established result that the LLs in valley K enjoy larger R_{xx} peaks to Fig. 4b, we can directly obtain the depicted LL structure. This allows us to label the valley polarizations of the quantum Hall states in Fig. 4a, as defined by $(n_K - n_{K'})/(n_K + n_{K'})$ with $n_{K,K'}$ is the number of electrons in valley K/K'. Figure 4c highlights a strong anticrossing at $\nu = 7$ (orange circle): the two anticrossed LLs of different valleys swap their relative positions abruptly with varying the density (dotted traces). Such LL anticrossings are most likely due to the formation of quantum Hall Ising ferromagnets driven by the exchange interaction¹²⁻¹⁴. This picture is consistent with the observation that the anticrossings at $\nu = 9$ and 11 are less pronounced, as the exchange interaction strength decreases with decreasing B or increasing the LL orbital index. Note that LL anticrossing is also observed for another density $n = 1.97 \times 10^{12} \text{ cm}^{-2}$ ($E_Z/E_c = 4$), as the dip at $\nu = 6$ (Fig. 3b).

Figure 4d shows the temperature dependence of the anticrossings. Clearly, the anticrossing gap at $\nu = 7$ disappears at ~ 3.3 K, whereas the single-particle gap at $\nu = 6$ disappears at a much higher temperature ~ 10.1 K. This provides further evidence for the many-body origin of the anticrossings. Moreover, the normalized R_{xx} at $\nu = 7$ exhibits a small peak at the shoulder, as pointed out by the arrow in the inset of Fig. 4d. Such an enhancement is reminiscent of those observed in the AIAs quantum well at much lower densities³³ and can be related to the charge transport along the domain wall loops near the first order Ising transition³⁴. Possible evolution and hysteresis^{33,35} of such a peak in future experiments at lower temperatures may completely decipher the anticrossings.

Figure 4e reveals the R_{xx} behavior under tilted magnetic fields. Away from the anticrossing, the R_{xx} features near $\nu = 6$ and 8 remain virtually unchanged for all accessible tilt angles. This insensitivity arises from the spin splitting and pinning to the out-of-plane direction, as explained above. By sharp contrast, on the two sides of the $\nu = 7$ anticrossing, the R_{xx} peaks do evolve with the tilt angle. The two peaks exchange their relative positions abruptly without eliminating the $\nu = 7$ minimum (dotted traces), corresponding to the reversal of Ising polarization. Such a tilt angle dependence implies that an in-plane magnetic field can couple the two LLs near their anticrossing, modify the exchange interaction, and tune the valley polarization of quantum Hall Ising ferromagnet.

In conclusion, we fabricate high-quality layer-polarized n -type MoS₂ devices and, for the first time, study valley-resolved SdH oscillations relevant to the spin-valley locked massive Dirac electron LLs. With decreasing density, we observe LL crossings and valley ferrimagnet-to-ferromagnet transitions, revealing a four fold enhancement of the valley Zeeman effect by the interactions. Near integer ratios of the Zeeman-to-cyclotron energies, we discover persistent LL anticrossings that can be attributed to the formation of quantum Hall Ising ferromagnets. The Ising valley polarizations appear to be reversible by tuning the density and in-plane magnetic field. Our results provide compelling evidence for strong many-body interaction effects in the conduction bands of monolayer MoS₂ and establish a fertile ground for exploring strongly correlated phenomena of massive Dirac electrons.

Methods

Sample preparation. Bulk MoS₂ crystals were purchased from 2D Semiconductors. To form the hBN/MoS₂/hBN sandwich structure, we employed a well-developed dry transfer technique: the MoS₂ flake was picked up by an hBN flake held by a polymethyl methacrylate (PMMA) film, which was then transferred onto a second hBN flake on a SiO₂/Si wafer^{24,25}. The stacked heterostructure was annealed at 300 °C in an argon-protected environment to reduce trapped interfacial bubbles. We used standard electron-beam (e-beam) lithography and reactive ion etching to pattern the Hall-bar structure and selectively etch away the top hBN at the contact areas. The e-beam lithography was performed again to define the electrodes. Ti/Au (5 nm/60 nm) electrodes were coated with e-beam evaporation. The number of layers of the MoS₂ flake was determined with optical contrast, atomic force microscopy (AFM), and Raman spectroscopy (see Supplementary Information for details).

Electrical measurement. A Stanford Research DS360 low-distortion function generator was used to apply a 4.5 Hz, 2 mV source-drain bias voltage. The current was measured by a Signal Recovery 7280 wide-bandwidth digital lock-in amplifier, and the longitudinal and Hall voltages were measured by Stanford Research SR830 lock-in amplifiers with SR550 voltage preamplifiers. The back gate voltage was provided by an Aim-TTi International PLH120 DC power supply. Electrical measurements were performed using a 15 Tesla Oxford Instruments superconducting magnet system with base temperature 1.5K, and using a 29 Tesla high-field system with base temperature 1.2 K at LNCMI-G.

1. Wang, Q. H., Kalantar-Zadeh, K., Kis, A., Coleman, J. N. & Strano, M. S. Electronics and optoelectronics of two-dimensional transition metal dichalcogenides. *Nature Nanotechnology* **7**, 699–712 (2012).
2. Xu, X., Yao, W., Xiao, D. & Heinz, T. F. Spin and pseudospins in layered transition metal dichalcogenides. *Nature Physics* **10**, 343–350 (2014).
3. Mak, K. F. & Shan, J. Photonics and optoelectronics of 2D semiconductor transition metal dichalcogenides. *Nature Photonics* **10**, 216–226 (2016).
4. Li, X., Zhang, F. & Niu, Q. Unconventional quantum Hall effect and tunable spin Hall effect in Dirac materials: application to an isolated MoS₂ trilayer. *Physical Review Letters* **110**, 066803 (2013).
5. Lu, J. M. *et al.* Evidence for two-dimensional Ising superconductivity in gated MoS₂. *Science* **350**, 1353–1357 (2015).
6. Xu, S. *et al.* Odd-integer quantum Hall states and giant spin susceptibility in p-type few-layer WSe₂. *Physical Review Letters* **118**, 067702 (2017).
7. Movva, H. C. P. *et al.* Density-dependent quantum Hall states and Zeeman splitting in monolayer and bilayer WSe₂. *Physical Review Letters* **118**, 247701 (2017).
8. Gustafsson, M. V. *et al.* Ambipolar Landau levels and strong exchange-enhanced Zeeman energy in monolayer WSe₂. *arXiv:1707.08083* (2017).

9. Xu, S. *et al.* Probing strong interactions in p-type few-layer WSe₂ by density-dependent Landau level crossing. *arXiv:1708.02909* (2017).
10. Zhu, J., Stormer, H. L., Pfeiffer, L. N., Baldwin, K. W. & West, K. W. Spin susceptibility of an ultra-low-density two-dimensional electron system. *Physical Review Letters* **90**, 056805 (2003).
11. Spivak, B., Kravchenko, S. V., Kivelson, S. A. & Gao, X. P. A. Colloquium: Transport in strongly correlated two dimensional electron fluids. *Reviews of Modern Physics* **82**, 1743 (2010).
12. Nicholas, R. J., Haug, R. J., Klitzing, K. v. & Weimann, G. Exchange enhancement of the spin splitting in a GaAs – Ga_xAl_{1-x}As heterojunction. *Physical Review B* **37**, 1294 (1988).
13. Jungwirth, T., Shukla, S. P., Smrčka, L., Shayegan, M. & MacDonald, A. H. Magnetic anisotropy in quantum Hall ferromagnets. *Physical Review Letters* **81**, 2328 (1998).
14. Girvin, S. M. Spin and isospin: Exotic order in quantum hall ferromagnets. *Physics Today* **53**, 39 (2000).
15. Mak, K. F., McGill, K. L., Park, J. & McEuen, P. L. The valley Hall effect in MoS₂ transistors. *Science* **344**, 1489–1492 (2014).
16. Wu, W. *et al.* Piezoelectricity of single-atomic-layer MoS₂ for energy conversion and piezotronics. *Nature* **514**, 470–474 (2014).

17. Zhang, Y. J., Oka, T., Suzuki, R., Ye, J. T. & Iwasa, Y. Electrically switchable chiral light-emitting transistor. *Science* **344**, 725–728 (2014).
18. Wang, Z., Shan, J. & Mak, K. F. Valley- and spin-polarized Landau levels in monolayer WSe₂. *Nature Nanotechnology* **12**, 144–149 (2016).
19. Wu, S. *et al.* Electrical tuning of valley magnetic moment through symmetry control in bilayer MoS₂. *Nature Physics* **9**, 149–153 (2013).
20. Lee, J., Mak, K. F. & Shan, J. Electrical control of the valley Hall effect in bilayer MoS₂ transistors. *Nature Nanotechnology* **11**, 421–425 (2016).
21. Liu, G.-B., Shan, W.-Y., Yao, Y., Yao, W. & Xiao, D. Three-band tight-binding model for monolayers of group-VIB transition metal dichalcogenides. *Physical Review B* **88**, 085433 (2013).
22. *See Supplemental Material .*
23. Wu, Z. *et al.* Even-odd layer-dependent magnetotransport of high-mobility Q-valley electrons in transition metal disulfides. *Nature Communications* **7**, 12955 (2016).
24. Wang, L. *et al.* One-dimensional electrical contact to a two-dimensional material. *Science* **342**, 614–617 (2013).
25. Xu, S. *et al.* Universal low-temperature Ohmic contacts for quantum transport in transition metal dichalcogenides. *2D Materials* **3**, 021007 (2016).

26. Pudalov, V. M., Gershenson, M. E. & Kojima, H. Probing electron interactions in a two-dimensional system by quantum magneto-oscillations. *Physical Review B* **90**, 075147 (2014).
27. Maryenko, D. *et al.* Spin-selective electron quantum transport in nonmagnetic MgZnO/ZnO heterostructures. *Physical Review Letters* **115**, 197601 (2015).
28. Cai, T. *et al.* Magnetic control of the valley degree of freedom of massive Dirac fermions with application to transition metal dichalcogenides. *Physical Review B* **88**, 115140 (2013).
29. Aivazian, G. *et al.* Magnetic control of valley pseudospin in monolayer WSe₂. *Nature Physics* **11**, 148–152 (2015).
30. Fang, F. F. & Stiles, P. J. Effects of a tilted magnetic field on a two-dimensional electron gas. *Physical Review* **174**, 823 (1968).
31. Piot, B. A. *et al.* Quantum Hall ferromagnet at high filling factors: A magnetic-field-induced Stoner transition. *Physical Review B* **72**, 245325 (2005).
32. Chen, X. *et al.* Probing the electron states and metal-insulator transition mechanisms in molybdenum disulphide vertical heterostructures. *Nature Communications* **6** (2015).
33. De Poortere, E. P., Tutuc, E., Papadakis, S. J. & Shayegan, M. Resistance spikes at transitions between quantum Hall ferromagnets. *Science* **290**, 1546–1549 (2000).
34. Jungwirth, T. & MacDonald, A. Resistance spikes and domain wall loops in Ising quantum Hall ferromagnets. *Physical Review Letters* **87**, 216801 (2001).

35. Piazza, V. *et al.* First-order phase transitions in a quantum Hall ferromagnet. *Nature* **402**, 638–641 (1999).

Acknowledgements This work is supported by the Research Grants Council of Hong Kong (Project No. 16300717, SBI17SC16), HKUST-UoM Seed Fund 2017, and UT-Dallas Research Enhancement Fund. We acknowledge the technical support from the Raith-HKUST Nanotechnology Laboratory for the electron-beam lithography facility at MCPF and the support of the LNCMI-CNRS, member of the European Magnetic Field Laboratory (EMFL).

Author contributions N.W., F.Z., and J.L. conceived the project. J.L. and T.H. fabricated and measured samples A,C, and sample B, respectively. J.L. and B.A.P. conducted high-field experiments at LNCMI-G. J.L. and F.Z. analyzed the data and the theoretical aspects. J.L. performed the fittings and prepared the figures. The remaining authors provided technical assistance in experimental measurements and analyses. J.L., F.Z., and N.W. wrote the manuscript, which was proofread by all authors.

Additional information Supplementary information is available in the online version of the paper. Correspondence and requests for materials should be addressed to F.Z. or N.W.

Competing Interests The authors declare no competing financial interests.

Figure 1

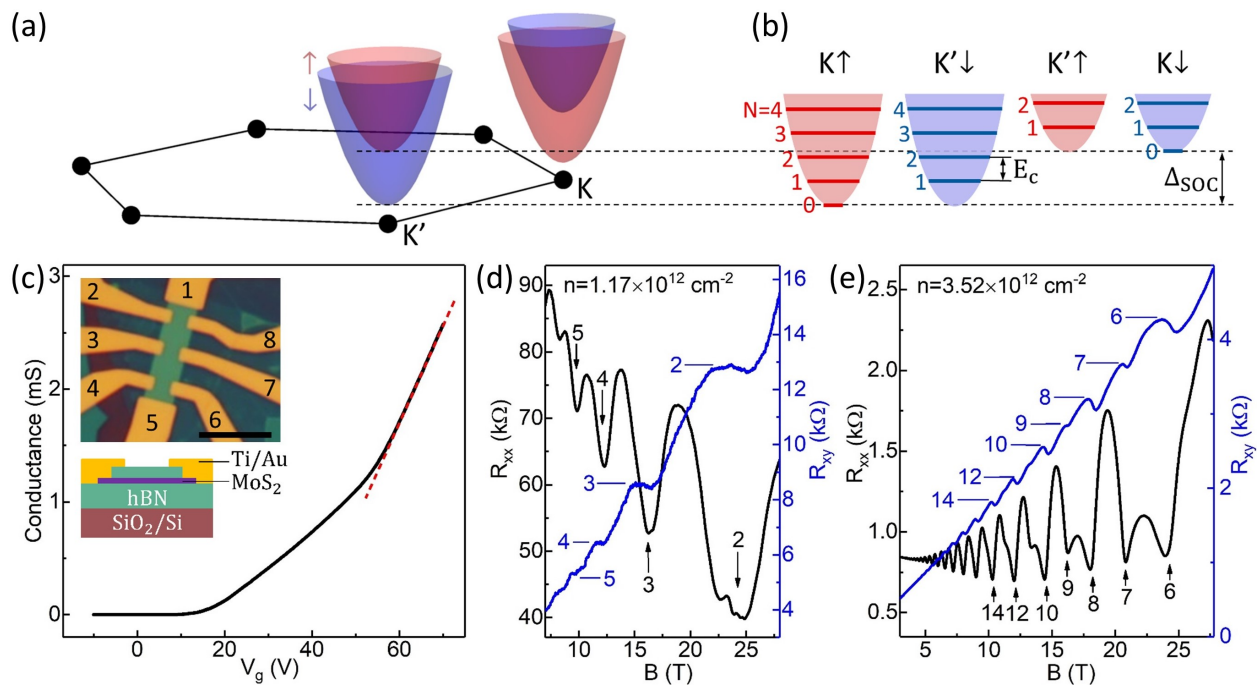


Figure 2

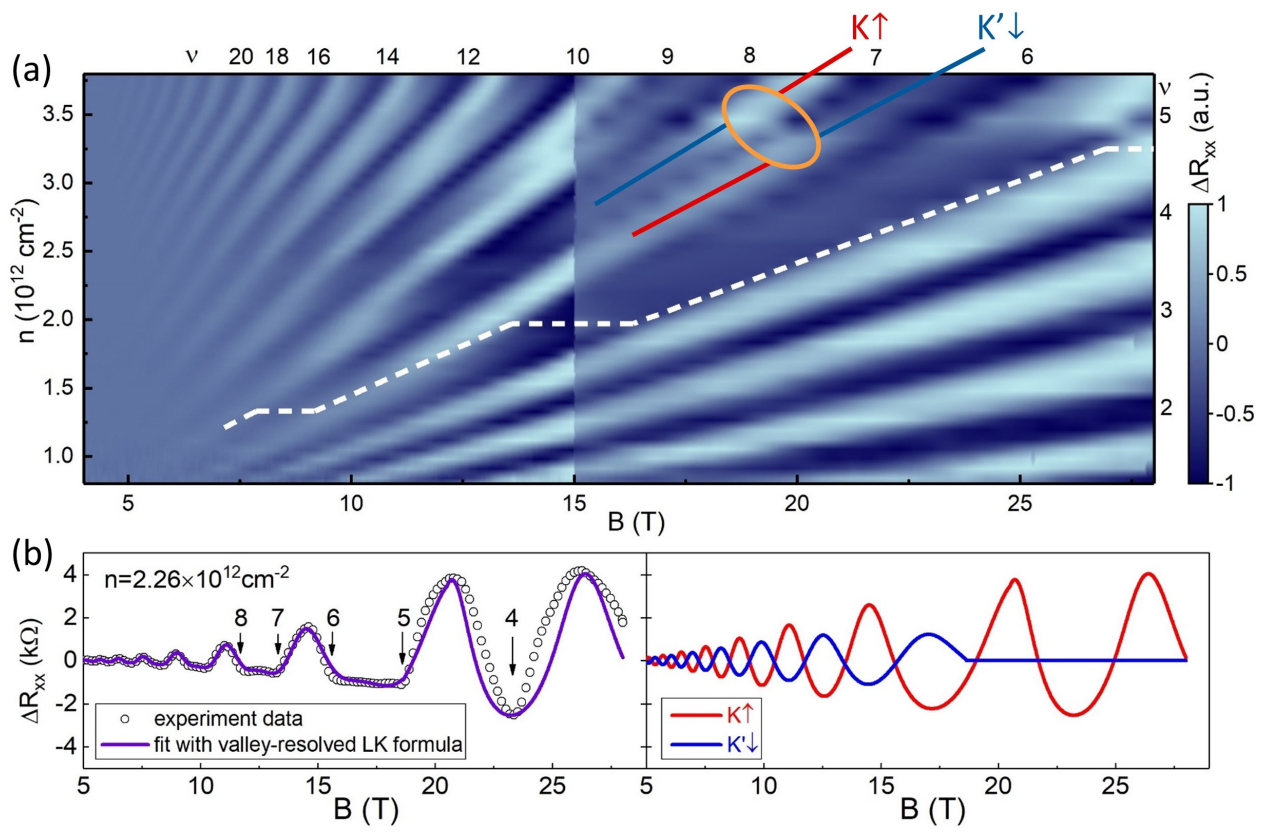


Figure 3

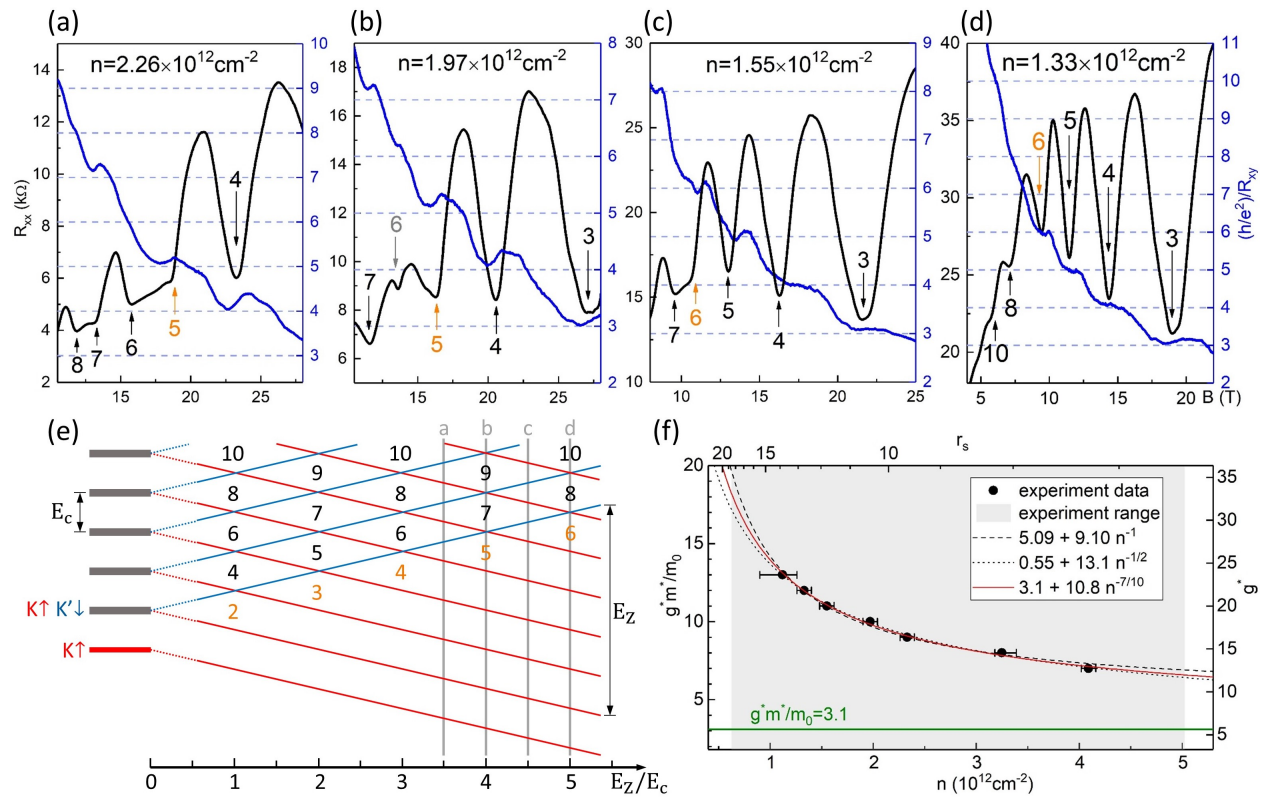


Figure 4

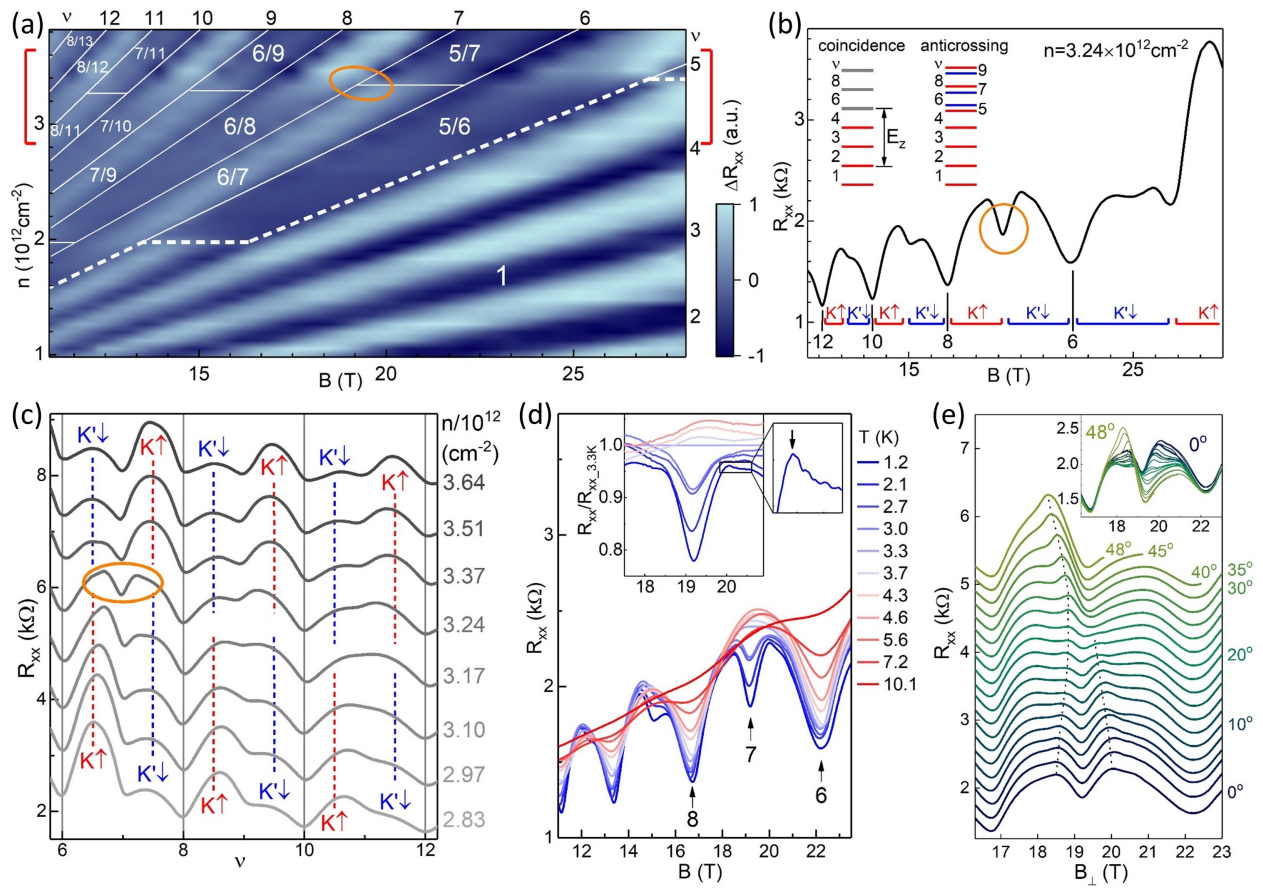


Figure 1 Band structure, device structure, field-effect conductance, and quantum oscillations of the layer-polarized MoS₂. (a) Hexagonal Brillouin zone of monolayer MoS₂ and its conduction band minima at K/K' points, with a splitting between the spin up (red) and spin down (blue) subbands. (b) Spin-valley locked conduction-band Landau level structure of massive Dirac electron bands, with Zeeman effect not considered. Δ_{SOC} is the spin splitting in each valley at zero magnetic field. (c) Four-probe FET conductance at 1.5 K. The red dashed line indicates an FE mobility of 22000 cm²/(V·s). Inset: the optical image and cross-section of the device, with a scale bar of 8 μm. (d) Magneto (black) and Hall (blue) resistance measured at 1.2 K at a low density, featuring quantized plateaus in Hall resistance. (e) The same as (d) but at a higher density, displaying a 2-to-1 valley degeneracy lifting.

Figure 2 Landau level fan diagram of the layer-polarized MoS₂. (a) Mapping of quantum oscillation amplitude in the $n - B$ space. The dark blue regions are R_{xx} minima, related to energy gaps in the density of states, whose corresponding filling factors are marked along the right and top edges. The data below and above 15 T were obtained in a 1.5 K superconducting cryogenic system and in a 1.2 K high magnetic field system, respectively, leading to the minor color discontinuity at 15 T. The red and blue solid lines mark a pair of crossing Landau levels with opposite spins and valleys, and the orange oval is the crossing position. The white dashed line marks the boundary between valley ferromagnetic and ferrimagnetic regimes. (b) Left: quantum oscillation data fitted with the valley-resolved LK formula. Right: two valley components of the fitting.

Figure 3 Density dependent valley Zeeman splitting. (a)-(d) R_{xx} (black) and $(h/e^2)/R_{xy}$ (blue) at different electron densities. (e) Schematics of Landau levels with increasing valley Zeeman splitting. The red and blue lines denote the valley K (spin-up) and valley K' (spin-down) Landau levels. Four vertical grey lines correspond to the situations in (a) to (d), respectively. Orange number labels ν_c that separates the valley ferrimagnetic and ferromagnetic regime. (f) Experimental values of g^* and g^*m^*/m_0 versus n and r_s . The horizontal error bars represent the uncertainty in V_g . Fittings with different formulas are shown.

Figure 4 Signatures of Landau level anticrossings. (a) Mapping of quantum oscillation amplitude in the $n - B$ space with valley polarizations labeled. (b) Quantum oscillations showing the valley-resolved Landau levels and their anticrossings. Inset: the corresponding Landau level structure. (c) R_{xx} versus ν at densities in the range marked by the red bracket in (a). The red and blue dashed lines mark the Landau levels in valley K and K', respectively. The orange ovals in (a)-(c) mark the same anticrossing at $\nu = 7$. (d) Temperature dependence of the anticrossing signatures in SdH oscillations. Inset: the normalized R_{xx} near $\nu = 7$. (e) Tilt angle dependence of the anticrossing at $\nu = 7$, offset for clarity. The dotted traces are guides to the eye for the positions of enhanced peaks in R_{xx} . Inset: the non-offset data.